Fully Resolved Simulations of Single Char Particle Combustion Using a Ghost-Cell Immersed Boundary Method

Kun Luo, Chaoli Mao, Jianren Fan, and Zhenya Zhuang
State Key Laboratory of Clean Energy Utilization, Dept. of Energy Engineering, Zhejiang University, Hangzhou 310027, P.R. China

Nils Erland L. Haugen
SINTEF Energy Research, Trondheim N-7465, Norway

Dept. of Energy and Process Engineering, Norwegian University of Science and Technology Kolbjørn Hejes vei 1B, Trondheim NO-7491, Norway

DOI 10.1002/aic.16136
Published online March 8, 2018 in Wiley Online Library (wileyonlinelibrary.com)

A novel ghost-cell immersed boundary method for fully resolved simulation of char particle combustion has been developed. The boundary conditions at the solid particle surface, such as velocity, temperature, density, and chemical species concentration, are well enforced through the present method. Two semiglobal heterogeneous reactions and one homogeneous reaction are used to describe the chemical reactions in the domain, and the Stefan flow caused by the heterogeneous reactions is considered. A satisfactory agreement can be found between the present simulation results and experimental data in the literature. The method is then used to investigate the combustion property of a char particle and the interaction between CO_2 gasification and O_2 oxidation. Furthermore, combustion effect on the exchange of mass, momentum and energy between gas- and solid- phase is explored. © 2018 American Institute of Chemical Engineers *AIChE J*, 64: 2851–2863, 2018
Keywords: immersed boundary method, ghost-cell, char combustion, fully resolved simulation

Introduction

Coal is one of the most available mineral resources used as a primary fuel for energy production. However, coal combustion has a serious environmental impact linked with the continuously increased emission of carbon dioxide, sulfur dioxide, nitrogen oxides, and fine particles into the atmosphere. To improve the design of combustion devices with enhanced combustion efficiency and reduced pollutant emission, it requires a deep understanding of the complex multiphysics and multiscale interactions coupled in the coal combustion process, as well as an accurate predictive capability of this process. With this background it is clear that, the investigation of the coal combustion process is of vital importance.

Char combustion plays an important role in the coal combustion process and a detailed understanding of the underling physical phenomena in the char combustion process is crucial for correct modeling of coal combustion. Typically, point particle models are used for simulation of particulate flow with char combustion in industrial devices. However, errors associate with these simplified char combustion submodels such as the single-film model proposed by Nusselt[1] and the double-film model,[2] need to be quantified and the constraints within which a given model is feasible should be assessed. Thus, a fully resolved numerical simulation method, in which the solid–gas interface and particle boundary layer are spatially and chemically resolved, is needed to describe the complete char combustion process.[3] Simulation results based on this method can be used to understand the underlying physical processes and to improve, assess and even develop new accurate models using point particle assumption for large-scale simulations. There are basically two approaches to implement the fully resolved simulation, including (1) body-conformal grid methods and (2) fixed-grid methods. As rapid particle moving/deforming processes are often involved in the char combustion process and the phase-interface changes correspondingly, frequent remeshing process will be needed in body-conformal grid methods, which will consume tremendous computer resources. Thus, a fixed-grid method will be more desirable in such a simulation.

The immersed boundary (IB) method is one of the fixed-grid methods and has been demonstrated to have the capability of handling complex fluid-structure interaction problems with high efficiency. The advantages of the IB method, such as simplicity in grid generation, savings in computer resources and straightforward parallelization, have expanded its applications in multiphase flow simulations.

The immersed boundary method was first introduced by Peskin[4] to simulate the blood flow around a human heart valve. The main idea of this method is to use a Cartesian

Additional Supporting Information may be found in the online version of this article.

Correspondence concerning this article should be addressed to J. Fan at fanjr@zju.edu.cn.

grid for fluid flow simulation together with a Lagrangian representation of the immersed boundary. A forcing term is introduced to represent the interaction between the immersed boundary and the fluid, and a discrete Dirac-delta function is used to smooth this singular force on the Eulerian grid.[5] As then, numerous modifications and improvements have been made, which are well discussed and categorized.[6–8] The idea of the ghost cell immersed boundary (GCIB) method is based on the work of Fadlun et al.[9] The GCIB method treats the immersed boundary as a sharp interface, and does not require the explicit addition of discrete forces in the governing equations, thus it can be easily combined with the existing solvers. The boundary condition on the IB is enforced through the "ghost cells." The variable values of the ghost cells are calculated with the IB boundary conditions and the fluid variables near the boundary. The flow solver senses the presence of the immersed boundary through the extrapolated values at the ghost points.[10] The GCIB method has shown large potential to handle different fluid–solid interaction problems, including those involving highly complex geometries[11–13] and moving/deforming objects.[14–16]

Extension of the immersed boundary method to heat transfer problems has gained its popularity as Kim and Choi.[17] Many researchers have paid their effort to improve the accuracy of immersed boundary methods and broaden its application in heat-transfer simulations. In our previous work,[18] a ghost-cell compressible IB method of second-order accuracy is designed to enforce Dirichlet, Neumann, and Robin type thermal boundary conditions. And an extension to complex phase-interface is made by Luo et al.[19] But until now, there are few studies about the immersed boundary method involving multiphase chemical reactions. McGurn et al.[20] investigated the conjugate heat-transfer and mass-transfer processes associated with charring solids. The moving interface is described by a level-set method and the boundary condition is enforced through a ghost-fluid methodology. The effects of surface blowing from off-gassing are superimposed through an explicit source term deposition into the Eulerian gas field. Kedia et al.[21] introduced a "buffer zone" methodology to simulate the reacting flow around a solid object. Their method imposes the conjugate boundary condition for heat transfer and nonpenetration boundary condition for species concentration on the immersed boundary and is able to track the flame around the object. Deen and Kuipers[22] extended the immersed boundary method to simulate infinitely fast heterogeneous reactions happened at the exterior surface of the particles, but the mass source caused by the surface reactions is not considered. As for other fix-grid methods, a new model to a track reacting particle interface and particle porosity has been presented very recently.[23] Simulation results there showed that the Stefan flow significantly modified the mass-transfer process governed by the Thiele modulus and the hydrodynamic boundary layer around the particle, indicating crucial importance of the particle-resolved combustion simulation. As the implementation of the immersed boundary for the gas–solid chemical reactions are still rare, it is desirable to develop an efficient IB method for multiphase combustion process.

The main objective of the present work is to develop a novel ghost-cell immersed boundary method for char combustion process based on the work of Luo et al.[18] The interaction between immersed body and the fluid is expressed by ghost points inside the immersed bodies, and these ghost points ensure that boundary conditions are satisfied precisely on the immersed boundary. Different reconstruction stencils are performed to enforce the boundary conditions of different variables.

The reminder of the present paper is organized as follows. The second and third sections describe the numerical methodology including the flow solver and the ghost-cell immersed boundary method for gas–solid chemical reactions. The fourth section describes the problem set-ups and some assumptions. In the fifth section, the capability of the proposed methodology to handle char combustion process is validated and further investigation is performed. The sixth section is devoted to discussions and conclusions.

Governing Equations

The continuity equation is solved in the form[24,25]

$$\frac{D\rho}{Dt}+\rho\nabla\cdot\boldsymbol{u}=\boldsymbol{0} \tag{1}$$

where ρ is the density, $\boldsymbol{u}$ is the fluid velocity, t is time, and $D/Dt=\partial/\partial t+\boldsymbol{u}\cdot\nabla$ is the convective derivative. The momentum equation is written in the form

$$\frac{D\boldsymbol{u}}{Dt}=\frac{1}{\rho}(-\nabla p+F_{vs}) \tag{2}$$

where p is the pressure

$$F_{vs}=\nabla\cdot(2\rho v\boldsymbol{S}) \tag{3}$$

is the viscous force, v is the kinematic viscosity and the traceless rate of strain tensor is

$$S_{ij}=\frac{1}{2}(\partial u_i/\partial x_j+\partial u_j/\partial x_i)-\frac{1}{3}\delta_{ij}\nabla\cdot\boldsymbol{u} \tag{4}$$

The equation for the mass fractions of each species is

$$\rho\frac{DY_k}{Dt}=-\nabla\cdot J_k+\dot{\omega}_k \tag{5}$$

where Y is the mass fraction. J is the diffusive flux, $\dot{\omega}$ is the reaction rate, and subscript k refers to species number. The calculation of the reaction rate $\dot{\omega}$ and diffusive flux J is based on the work of Babkovskaia et al.[25]

Finally, the energy equation is

$$\left(c_p-\frac{R}{m}\right)\frac{D\ln T}{Dt}=\sum_k\frac{DY_k}{Dt}\left(\frac{R}{W_k}-\frac{h_k}{T}\right)-\frac{R}{W_{\mathrm{mix}}}\nabla\cdot\boldsymbol{u}+\frac{2vS^2}{T}-\frac{\nabla\cdot\boldsymbol{q}}{\rho T} \tag{6}$$

where T is the temperature, c_p is the specific heat at constant pressure, R is the universal gas constant, h is the enthalpy, m is the molar mass, and $\boldsymbol{q}$ is the heat flux. In this work, we use the ideal gas equation of state given by

$$p=\frac{\rho RT}{m} \tag{7}$$

to enclose above equations.

Besides, the kinematic viscosity v in Eq. 2 is calculated as[26]

$$v=\frac{1}{\rho}\sum_{k=1}^{\text{nspec}}\left[x_k\mu_k/\sum_{j}^{\text{nspec}}\left(x_j\left(\frac{1}{2\sqrt{2}}\frac{1}{\sqrt{1+m_k/m_j}}\left(1+\sqrt{\frac{\mu_k}{\mu_j}}*\left(\frac{m_k}{m_j}\right)^{-0.25}\right)^2\right)\right)\right] \tag{8}$$

where x_k is the species' mole fraction in the gas mixture and the dynamic viscosity of a given species μ_k is a function of local temperature as[27]

$$\mu_k=\frac{5}{16}\frac{\sqrt{\pi k_B T m_k}}{\pi\sigma_k^2\Omega_k^{(2,2)_*}} \tag{9}$$

where σ_k is the Lennard-Jones collision diameter, k_B is the Boltzmann constant

$$\Omega_k^{(2,2)_*}=\Omega_{L-J}^{(2,2)_*}+0.2\delta_k^*/T_k^* \tag{10}$$

is the collision integral,[28] in which

$$\Omega_{L-J}^{(2,2)_*}=\left[\sum_{i=0}^{7}a_i\left(\ln T_k^*\right)^i\right]^{-1} \tag{11}$$

is the Lennard-Jones collision integral and

$$\delta_k^*=\frac{v_k^2}{2\varepsilon_k\sigma_k^3},\ T_k^*=\frac{k_B T}{\varepsilon_k} \tag{12}$$

are the reduced dipole moment and temperature, respectively. And ε_k is the Lennard-Jones potential well depth and v_k is the dipole moment. Both of them should be given as input together with σ_k. The coefficients a_i can be found in the paper.[25]

In Eq. 4, the heat flux $\boldsymbol{q}$ is given by

$$\boldsymbol{q}=\sum_k h_k J_k-\lambda\nabla T \tag{13}$$

where the thermal conductivity λ is found from the thermal conductivities of the individual species as

$$\lambda=\frac{1}{2}\left(\sum_k^{\text{nspec}}x_k\lambda_k+1/\sum_k^{\text{nspec}}x_k/\lambda_k\right) \tag{14}$$

in which the individual species conductivities

$$\lambda_k=\frac{v_k}{m_k}\left(f_{\text{trans}}C_{v,\text{trans}}+f_{\text{rot}}C_{v,\text{rot}}+f_{\text{vib}}C_{v,\text{vib}}\right) \tag{15}$$

are composed of transitional, rotational,[25] and vibrational contributions.[29]

The enthalpy of the ideal gas mixture, as used in Eq. 4, can be expressed in terms of isobaric specific heat and temperature as

$$h_k=h_k^0+\int_{T_0}^{T}c_{p,k}dT,\quad h=\sum_k^{\text{nspec}}Y_k h_k \tag{16}$$

The heat capacity is calculated using a Taylor expansion

$$c_p=\frac{R}{m}\sum_{i=1}^{5}\alpha_i T^{i-1} \tag{17}$$

where α_i can be found in the CHEMKIN manual.[30]

Ghost-Cell Immersed Boundary Method for Char Combustion

In the previous work,[18] we have proposed a ghost-cell compressible immersed boundary method (GCCIB) which is capable of handling Dirichlet, Neumann, and Robin boundary conditions. In the present work, this method is further developed to involve chemical reaction inducing mass-transfer processes. Its easy implementation enables us to use the existing solver of the PENCIL CODE[24] without modifying the governing equations.

In heterogeneous combustion context, the coupling among the boundary velocity, temperature, and the species mass fraction is complicated. Especially, surface reactions affect mass and energy balance at the gas–solid interface, and thus have an important influence on the boundary conditions. Therefore, the most difficult thing is to determine the proper IB boundary conditions and then enforce them to the flow field in the present method. A detailed description of the corresponding strategy can be found in the following introductions.

A brief schematic of the reconstruction scheme in the GCCIB method[18] is shown in Figure 1. Three layer of ghost points is chosen to construct a six-order central finite difference. Under Dirichlet boundary condition, for example, velocity and given temperature boundary conditions, a local second-order accurate extrapolation for the ghost point can be obtained using only the mirror point together with the BI point. While for Neumann and Robin boundary condition, for example, nonpenetration, given heat flux and chemical species boundary conditions, instead of the mirror point, two probe points are needed to maintain the second-order accuracy. More details can be found in our previous work.[18]

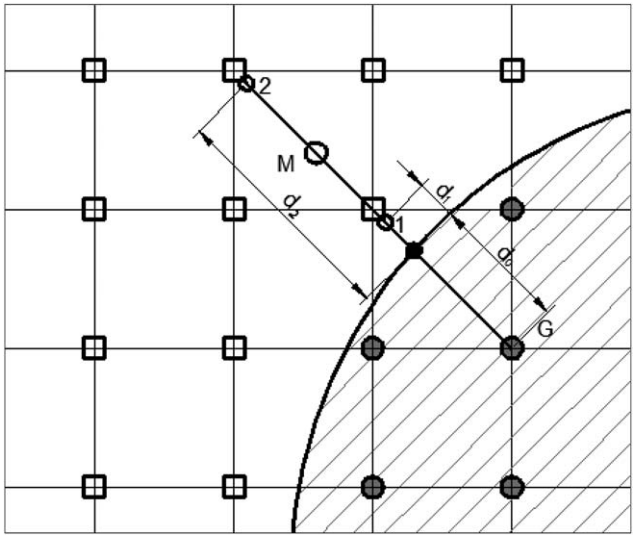

Figure 1. Extrapolation implementation for the present ghost-cell immersed boundary method.

(●: ghost points, ○ (M): mirror points, ○ (1, 2): probe points, ●: boundary intersection (BI) points, □: fluid points).

The velocity at the immersed boundary

The convective and diffusive mass flux of gas-surface species at the surface are balanced by the production (or depletion) rate of gas phase species by surface reactions. This relationship is

$$\overline{n} \cdot \left[\rho Y_k(\overline{V_k}+\overline{u})\right]=\dot{S}_k W_k, \tag{18}$$

where $\bar{n}$ is the outward-pointing unit vector that is normal to the surface and $\dot{S}_k$ is the molar production rate of the kth species. Here, the gas-phase diffusion velocities are related to the gradients of species mass fraction by

$$\overline{V_k}=\frac{1}{X_k\overline{W}}\sum_{j\neq k}^{K_g} W_j D_{k,j}\nabla X_j \tag{19}$$

and can be calculated from the species transport equation with

$$\sum_k V_k Y_k=0 \tag{20}$$

being a constraint for diffusion velocities of different species. The induced Stefan flow velocity is given by

$$\overline{n} \cdot \overline{u}=\frac{1}{\rho}\sum_{k=1}^{K_g}\dot{m}_k \tag{21}$$

During char combustion process, the char particle keeps shrinking and its boundary moving velocity, which is in the normal direction to the boundary, can be calculated as

$$v_n=\frac{dr_s}{d\tau}=\frac{\int_{\text{surf}}\dot{m}_C ds}{\pi r_s \rho_C} \tag{22}$$

The velocity at the interface is a combined effect of Stefan flow velocity and the particle shrinking velocity

$$u_{IB}=\overline{u}+v_n \tag{23}$$

As the velocity at the immersed interface is now a known variable, the ghost point velocities can then be calculated using a linear interpolation as

$$u_G=\frac{(d_0+d_1)u_{IB}-d_0 u_M}{d_1} \tag{24}$$

where u_M is the velocity value on mirror point. The definition of d_0 and d_1 can be found in Figure 1.

The temperature of the immersed boundary

By neglecting the temperature gradient within the particle, the diffusive heat flux in the gas phase is balanced by thermal radiation, chemical heat release and heat conduction from the gas phase to the solid surface, such that

$$Vc_{p,C}\frac{dT_p}{d\tau}=\int_{\text{Surf}}\left(-\sigma\varepsilon(T_p{}^4-T_0^4)+\sum_{k=1}^{K}\dot{m}_k h_k+\overline{n}\cdot\lambda\nabla T_{\text{gas}}\right)ds \tag{25}$$

where V is the volume of the object and the integral on the right-hand side is over the external surface of the object while ds is a surface element. T_0 is the temperature of surrounding gas. The calculation of the enthalpy is based on the form used in CHEMKIN.[30] In this work, Eq. 18 is solved explicitly to only obtain the time history of particle temperature and not to implement the thermal boundary conditions. On the chemically reacting surface, the temperature gradient should be prescribed,[31] that is, a Neumann type temperature boundary condition is necessary.

The enforcement of species boundary condition

Species concentrations are unknown variables at the immersed interface. Due to the fact that heterogeneous reactions affect the mass and energy balance at the interface, they have a significant influence on the boundary conditions both for the gas species and for the temperature.

The convective and diffusive mass fluxes of the gas phase species at the particle surface are balanced by the production/destruction rates of gas phase species by surface reactions

$$\rho D_k \bar{n}\cdot\nabla Y+\dot{m}_c Y_k+\dot{m}_k=0 \tag{26}$$

where the first term represents the diffusive mass flux while the second term is the convective mass flux and $\dot{m}_k$ is the mass production rate of the kth species. A detailed deduction of Eq. 26 can be found in Supporting Information Appendix B. The diffusion coefficient D_k is calculated in a simple way as CHEMKIN[30]

$$D_k=\frac{D_{\text{const}}}{\rho}\cdot\left(\frac{T_{IB}}{T_{\text{ref}}}\right)^{0.7}\cdot\frac{1}{Le_k} \tag{27}$$

where $D_{\text{const}}=2.58\times10^{-4}\text{kg}/(\text{m}\cdot\text{s})$ and $T_{\text{ref}}=298\text{K}$.

According to Eq. 26, the species at the burning boundary follows the representation of Robin type boundary condition. The only unknown parameters are the mass production rates $\dot{m}_C$ and $\dot{m}_k$. As $\dot{m}_C$ and $\dot{m}_k$ are coupled with the species mass fraction Y_k, Eq. 26 is supposed to be solved implicitly. While in the present work, the mass fraction Y_k at the immersed boundary is calculated by bilinear-interpolate the mass fraction of current time-step on surrounding fluid points, which means that Eq. 26 is solved explicitly here. Details about the calculation of mass fractions at the ghost point can be found in Supporting Information Appendix B.

The enforcement of pressure boundary condition

The pressure gradient in the vicinity of the immersed boundary needs to be zero to fulfill the nonpenetration condition and this is implemented through the reconstruction of the density by applying the equation of state. A second-order expression can be written as

$$\rho_G=\frac{m_G}{T_G}\left[\frac{\rho_1 T_1}{m_1}+\frac{d_0^2-d_1^2}{d_2^2-d_1^2}\cdot\left(\frac{\rho_2 T_2}{m_2}-\frac{\rho_1 T_1}{m_1}\right)\right] \tag{28}$$

where the subscript G denotes ghost point and 1(or 2) indicates the information on the first (or the second) probe point. d_0, d_1, and d_2 are defined in Figure 1. The calculation of the ghost point density can be found in Supporting Information Appendix B.

A summary of the present method

In every time step, the novel ghost cell immersed boundary method for gas-solid multiphase combustion can be summarized as follows:

Detect the position of the immersed interface and identify the ghost points, boundary intersection points, mirror points, and probe points;

1. Calculate the production rate $\dot{m}_C$ and $\dot{m}_k$ at the immersed boundary using the Arrhenius equation and get the

Table 1. Reaction Kinetic Constants

		$K=B\exp(-E/RT)$		
Chemical Reaction		B	E(J/mol)	Reference
R1	$2C+O_2 \rightarrow 2CO$	1.97×10^7	1.98×10^5	Zhang et al.[32]
R2	$C+CO_2 \rightarrow 2CO$	1.291×10^5	1.91×10^5	Zhang et al.[32]
R3	$2CO+O_2 \rightarrow 2CO_2$	2.24×10^{12}	1.6742×10^5	Nikrityuk et al.[33]

mass fractions at the ghost points with the Robin type reconstruction scheme;

2. Calculate the Stefan flow velocity and particle shrinking velocity with the production rate $\dot{m}_C$ and $\dot{m}_k$;

3. The particle temperature at the next time step can be found explicitly through Eq. 25, using the temperature of the present time step in the RHS of the equation;

4. Compute the ghost cell values for all variables and update the particle radius according to the particle shrinking velocity.

Problem and Assumptions

In the present work, a single cylindrical char particle, placed in a free gaseous flow, was considered. The chemistry was modeled using semiglobal homogeneous and heterogeneous reactions written as follows.

Heterogeneous reactions

$$2C+O_2 \rightarrow 2CO \tag{29}$$

$$C+CO_2 \rightarrow 2CO \tag{30}$$

Homogeneous reaction

$$2CO+O_2 \rightarrow 2CO_2 \tag{31}$$

The reaction kinetics parameters are listed in Table 1.

The heterogeneous char reaction rates are assumed to be of first order both in oxygen and carbon dioxide concentration. Hence, the reaction rates of O_2, CO_2, and CO due to the heterogeneous reactions can be written as

$$\dot{m}_{O_2} = -\rho Y_{O_2} B_1 \exp\left(-\frac{E_1}{RT_p}\right) \tag{32}$$

$$\dot{m}_{CO_2} = -\rho Y_{CO_2} B_2 \exp\left(-\frac{E_2}{RT_p}\right) \tag{33}$$

$$\dot{m}_{CO} = -2\left(\frac{M_{CO}}{M_{O_2}}\dot{m}_{O_2} + \frac{M_{CO}}{M_{CO_2}}\dot{m}_{CO_2}\right) \tag{34}$$

Then, the char conversion rate can be calculated as

$$\dot{m}_C = 2\frac{M_C}{M_{O_2}}\dot{m}_{O_2} + \frac{M_C}{M_{CO_2}}\dot{m}_{CO_2} \tag{35}$$

To simulate the char conversion process with the present ghost-cell immersed boundary method, several assumptions and simplifications are needed, which are listed below.

1. The porosity of the particle is incorporated into the pre-exponential factors of the heterogeneous reactions;[34]

2. The cross section of particle is circular during the shrinking process;

3. The particle consists of carbon only;

4. The temperature gradient within the particle is neglected;

5. The gaseous environment only consists of N_2, O_2, CO, and CO_2. Water vapor is taken into account by having an effect on the CO oxidation reaction;[34]

6. The gas radiation is not taken into account.

In the present simulation, the particle oxidation only happens at the particle surface. The shape of the particle remains circular during the shrinking process for easy interface tracking. According to these assumptions, the chemical reactions only happen at or outside the solid-fluid interface.

Numerical results

Convergence Test. As the spatial accuracy for no-slip velocity, nonimpermeable pressure and Dirichlet, Neumann and Robin thermal boundary conditions has been presented in our previous work,[18] we focus on the Robin type reactive boundary condition in this paper.

The case of a 2D char particle burning in a quiescent atmosphere is conducted to verify that the present scheme is of second-order spatial accuracy. The solid particle is located at the center of a square computational domain with the size of $10d\times10d$(d is the diameter of the cylinder). A series of grid resolutions (400×400, 600×600, 800×800, and 1600×1600) are used to calculate the same problem. Periodic boundary conditions are enforced on both the streamwise and spanwise directions. We choose a relatively small-time step of 2×10^{-8}s and integrate the solution to the same instant (0.01s) for all resolutions. The results with the highest resolved grid of 1600×1600 is used as a baseline.

Figure 2 shows the variation of the norms of relative errors and indicates the accuracy of the scheme. The mass fractions of species N_2, CO, and CO_2 (not considering O_2 is due to the almost zero value because O_2 is consumed completely in the CO flame sheet) in the vicinity of the solid surface are used to calculate the L_2-norm errors, because we mainly cares about

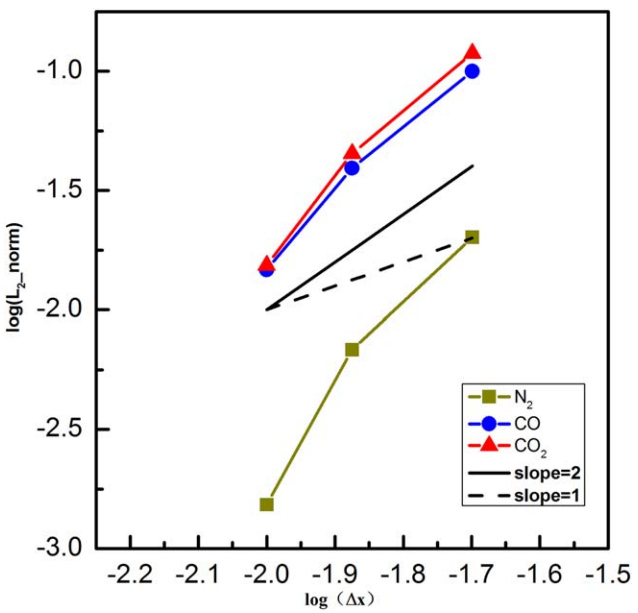

Figure 2. L_2-norms computed at different grid levels.

[Color figure can be viewed at wileyonlinelibrary.com]

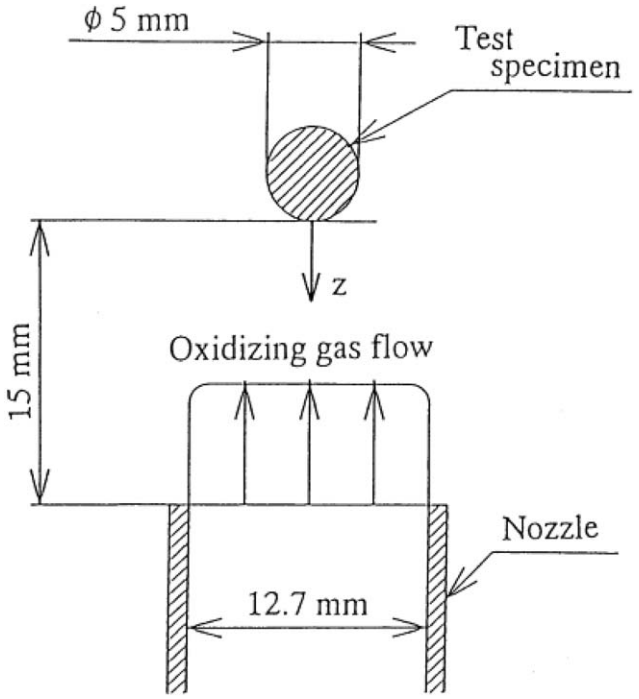

Figure 3. Schematic of the experiment by Makino et al.[35]

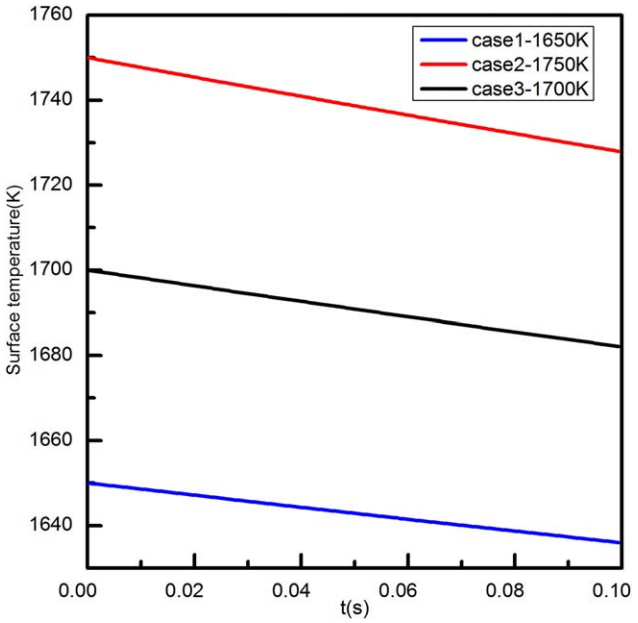

Figure 5. Temperature evolution of the graphite rod during combustion.

[Color figure can be viewed at wileyonlinelibrary.com]

the accuracy near the IB. As we can see from Figure 2, the second-order convergence accuracy is achieved for all species.

Validation. In the previous work,[18] the ability of the present method to handle Dirichlet, Neumann and Robin type thermal boundary condition has been validated. In this section, the GCCIB method is first used to simulate the experiment conducted by Makino et al.[34] for validation of its capability to deal with a reacting surface. Figure 3 describes the experimental setup, where a graphite rod with the diameter$d=5$mm and density $\rho=1.25\times10^3\mathrm{kg/m}^3$ is placed in air atmosphere. The hot oxidizing gas flows toward the cylinder at different speeds and the average consumption rate of the specimen is measured.

In the simulation, a large $20d\times16d$ computational domain (see Figure 4) is adopted to minimize domain confinement effects and the grid resolution is chosen to be $\Delta x=1/50d$. The inlet temperature of the oxidizing gas is set to be 1280 K and the incoming velocity is defined by the velocity gradient $a=4V_\infty/d$, which is $820s^{-1}$ in the current paper. The pressure

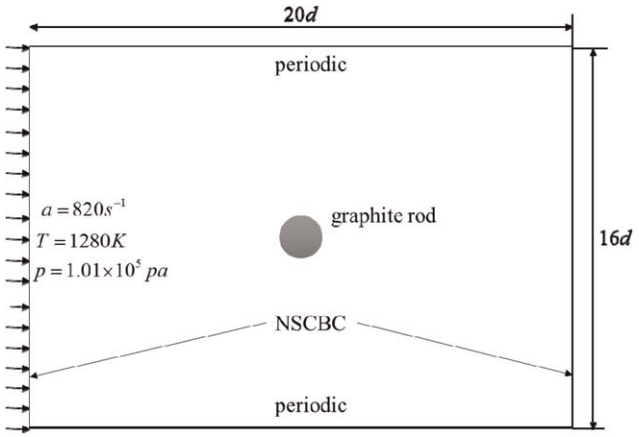

Figure 4. Schematic of computational domain.

at the inlet is $p_0=1.01\times10^5Pa$. As shown in Figure 4, NSCBC[36] boundary conditions are applied at both the inlet and outlet boundary while periodic boundary conditions are used for the span wise direction. Every simulation runs for 0.1 s so that a quasisteady state can be obtained.

First, the evolution history of the temperature of the graphite rod is investigated in Figure 5. As can be seen, the temperature keeps decreasing during the simulation and the amplitude is within 30 K, as a result of the energy balance of reactive heat release, conduction, convection and radiation heat transfer. This was confirmed by the experimental observation of Makino et al.[34] that the rod needed to be heated by a resistive heater to remain at a constant temperature. Therefore, in the following simulations, the solid surface temperature is fixed.

In Figure 6, the conversion rate of the carbon cylinder, calculated by the current method, is compared with the experimental measurement and analytical results.[34] In view of all the assumptions and uncertainties, the error is acceptable. Moreover, one can see that with the increase of surface temperature, the combustion rate first increases, then decreases, and then increases again. This transition phenomenon in the variation of carbon burning rate with the increase of surface temperature is accurately captured and the critical temperature is about 1700 K, which is agreeing well with the experimental result.

There are various explanations for this transition phenomenon, such as the "site" theory[35] and the change of reaction depth at constant activation energy.[37] Makino et al.,[38] however, attributed it to a change of the dominant surface reaction from R1 (2C-O_2->2CO) to R2 (C-CO_2->2CO), which is caused by the appearance of a CO flame over the burning carbon. With the current access to fully resolved simulations of the relevant cases, the underlying physical reason for the transition phenomena is explored.

Figure 7 shows the CO flame in terms of the consumption rate of carbon monoxide by the homogenous reaction. With the increase of surface temperature, a CO flame starts to form

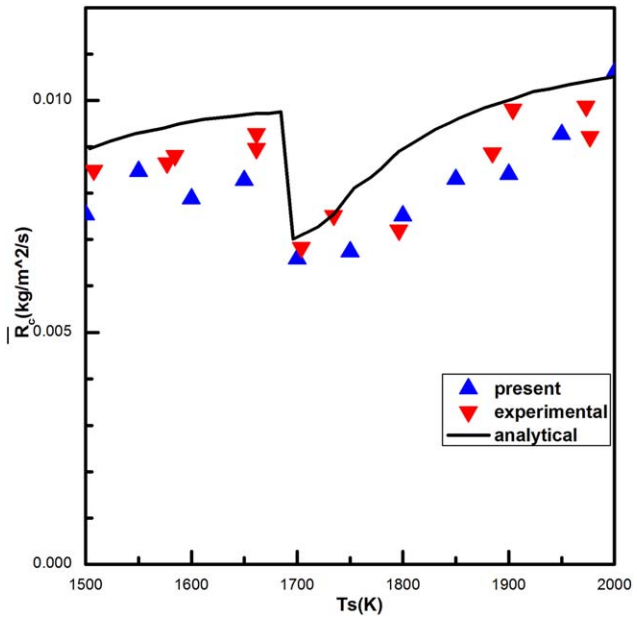

Figure 6. Carbon burning rate at different surface temperatures.

[Color figure can be viewed at wileyonlinelibrary.com]

in front of the cylinder and then wraps the rod while staying attached to the solid surface. When the surface temperature exceeds 1700 K, the flame first detaches from the rear of the rod and then from the front. Finally, a CO flame sheet is formed around the solid surface at a given distance. It prevents the oxygen from diffusing to the carbon surface, and hence, causes an increase in the relevance of R2 at the expense of R1. The change of the flame structure is a result of the competition between the incoming flow and the Stefan flow. Figure 8 shows the respective contribution of O_2 and CO_2 to the production of CO in heterogeneous reactions. The transition from solid carbon oxidation to gasification is evident. Present results agree well with Makino's conclusions.[38] This provides a validation of the applicability of the present surface resolved IB method for detailed descriptions of char particle conversion.

Study of Transport and Chemistry Interactions. In this section, the influence of the flow field on properties of single char particle conversion will be investigated by analyzing results from cases with different particle Reynolds numbers. Then, the effect of the char conversion on particle drag force and heat transfer with surrounding fluid will be studied. Both of the above points are of vital importance in modeling reactive particulate flows.

The particle Reynolds number is varied from 2.5 to 30.0 (Re = 2.5, 5, 7.5, 8, 15, 20, 25, 30.0.), by changing the velocity of the incoming flow. The lower range (2.5–8.0) of the Reynolds number is chosen based on the conditions in Aachen's 100 kW swirl burner.[39] What demand add is that, the diameter is set to be 5 mm in the present simulation. Although this does not match the condition in Aachen swirl burner where the particle size ranges from 4.5 to 435 um, we keep the dimensionless Reynolds number the same using the nondimensionalization. For investigation of the drag force and heat transfer, this is meaningful. The upper range (8.0–30.0) is to make a full use of current simulation data. The solid surface temperature is fixed at 1500 K to keep the gas reaction zone constrained near the solid surface. Otherwise, the simulation setup is the same as that described in the validation section. Each simulation runs for 0.1 s to ensure that a quasi-steady state has been obtained. Density, porosity and diameter variations can be neglected for this small-time period compared with the whole burnout time.

Conversion Properties Under Different Reynolds Numbers. In this section, both char conversion and the gas phase reactions are analyzed. The influence of particle Reynolds number on the averaged consumption rate over the surface of the char particle is plotted in Figure 9. An increase of the char conversion rate with increasing Reynolds number can be observed, as is also found by Richter et al.[40] Because the temperature of the solid surface is fixed, we explore the behind reasons by quantifying the mass fraction of different species at the solid surface in Figure 10. As can be seen, with the increase of Reynolds number, the averaged concentration of oxygen over the solid surface increases while the concentration of carbon dioxide decreases. As char conversion due to oxidation dominates within the current range of Reynolds number, an increase of the conversion rate is reasonable. Due

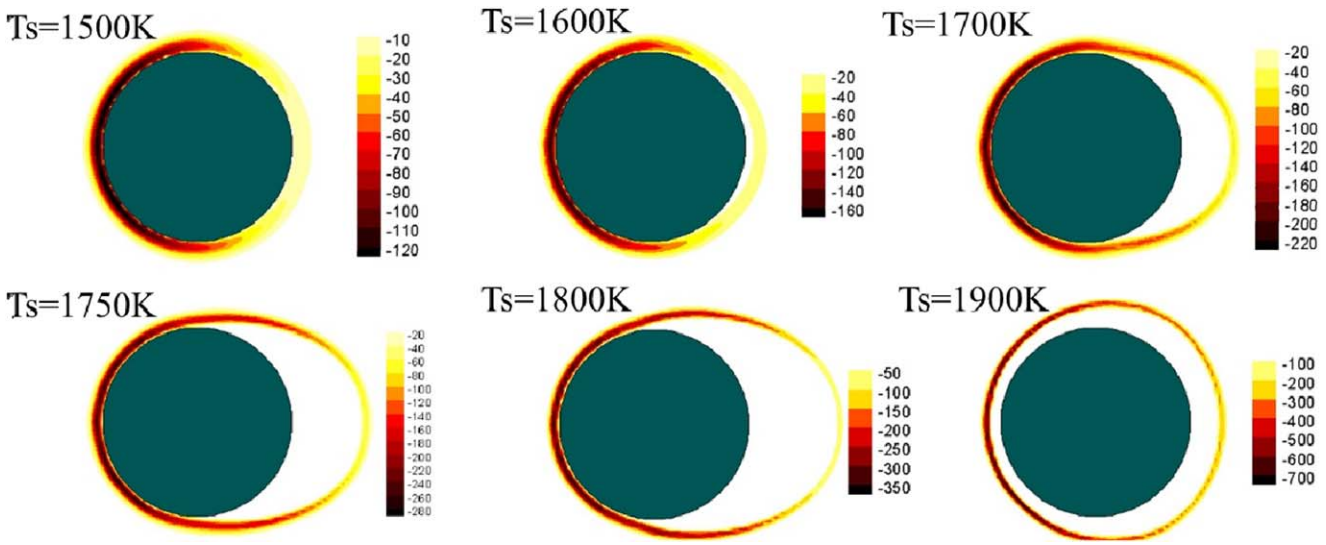

Figure 7. CO flame around the burning carbon surface at different temperatures.

[Color figure can be viewed at wileyonlinelibrary.com]

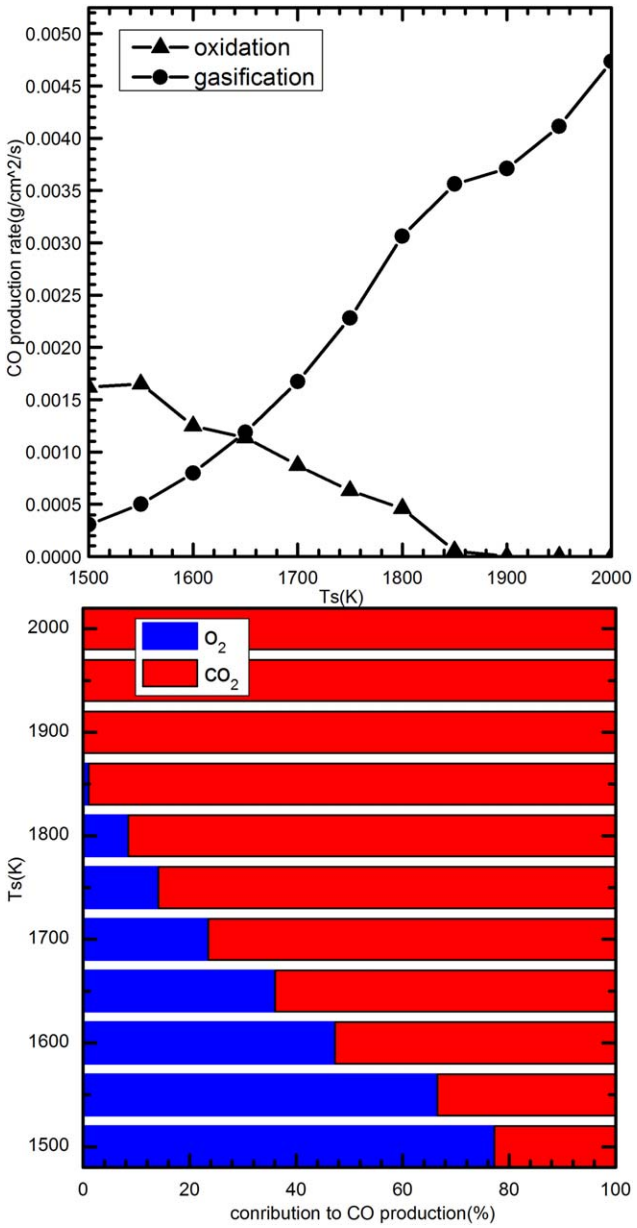

Figure 8. The dominant surface reaction changing from R1 (2C-O_2->2CO) to R2 (C-CO_2->2CO).

[Color figure can be viewed at wileyonlinelibrary.com]

to the relatively high activation energy of the gasification reaction, it could be expected that at higher surface temperature, when the relative importance of gasification increases (see Figure 8), the Reynolds number trend shown in Figure 7 will be weakened. To understand the underlying reasons that result in such a distribution of oxygen and carbon dioxide, the respective diffusive and convective fluxes of O_2 and CO_2 are investigated. Both of the two quantities are averaged over the particle surface and defined as positive away from the interface. Figure 11 shows the variation of these quantities with increasing Reynolds numbers. It can be observed that diffusion dominates for the transportation of oxygen toward the surface while convection takes advantage over diffusion to transport carbon dioxide away from the fluid-solid interface. As a higher Reynolds number means faster transportation of oxygen from the incoming flow to the border of the burning boundary layer and also thinner boundary layer, which leads to sharper

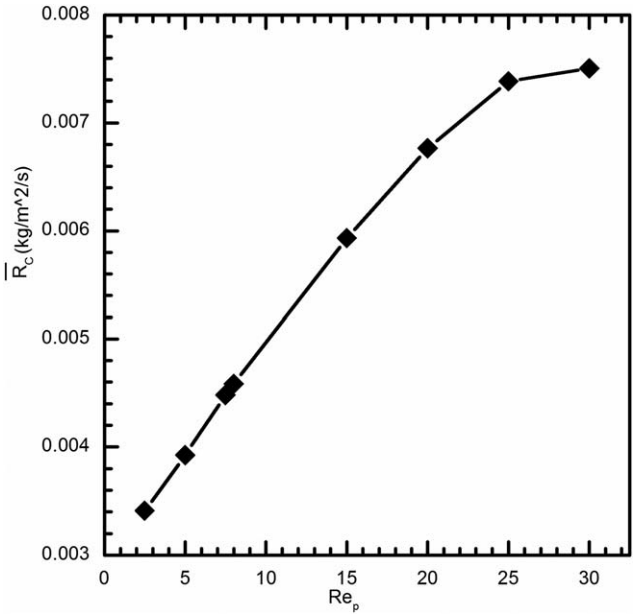

Figure 9. Evolution of averaged char consumption rate versus Reynolds number.

gradient of the concentration of O_2, a rapid diffusion of O_2 through the layer can be expected. As a result, the carbon is consumed more rapidly, resulting in a faster Stefan flow (see Eq. 21). This contributes significantly to the convection of CO_2 away from the solid surface. Moreover, one can see that carbon monoxide is transported away from the solid surface by both convection and diffusion, indicating that the heterogeneous reactions are providing reactants to the gas-phase reaction.

Similar to the effect of an increasing surface temperature, the increasing particle Reynolds number also contributes to a change in the relative importance of the oxidation and gasification reactions, which can be seen in Figure 12. This is a result of a different dominant factor (for the respective transportation of O_2 and CO_2). High Reynolds number increases the diffusion of oxygen to the solid surface while the resulting faster Stefan flow transports more carbon dioxide away from

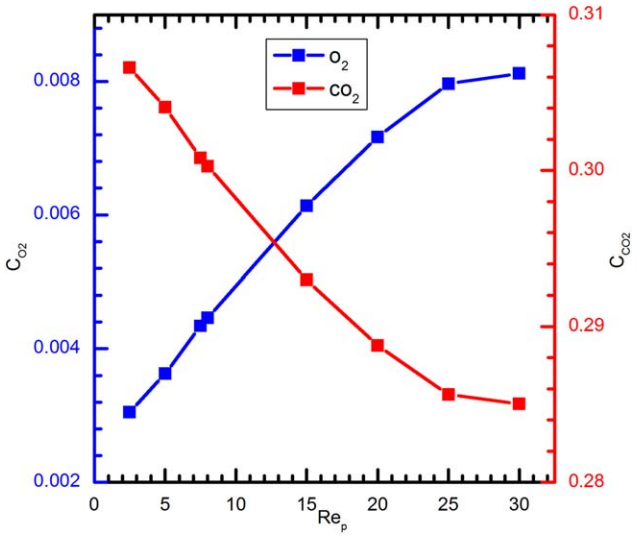

Figure 10. The averaged concentration of O_2 and CO_2 under different Re_ps.

[Color figure can be viewed at wileyonlinelibrary.com]

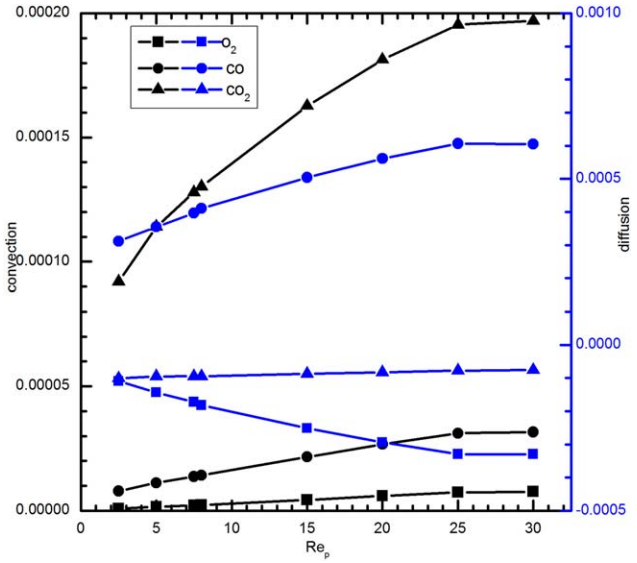

Figure 11. The influence of Reynolds number on averaged transportation.

[Color figure can be viewed at wileyonlinelibrary.com]

the surface. Figure 12 also implies that the single-film model is appropriate for char particle combustion when the Reynolds number is high.

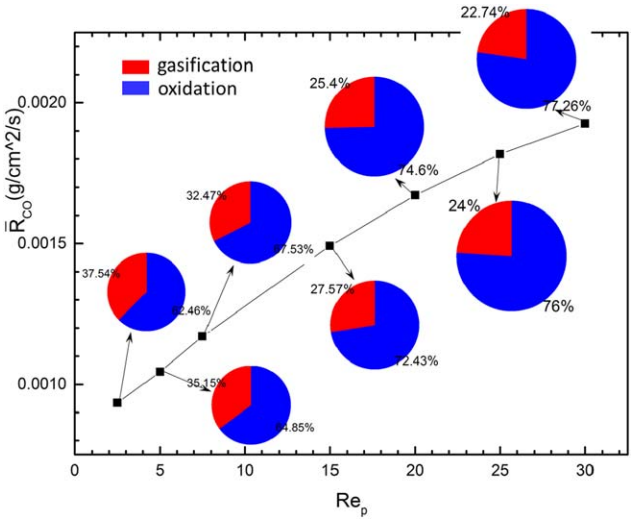

Figure 12. Respective contribution of O_2 and CO_2 to the production of CO on the surface.

[Color figure can be viewed at wileyonlinelibrary.com]

The reaction zones of the gas phase for different Reynolds numbers are shown in Figure 13 in terms of the consumption rate of carbon monoxide by the homogenous reaction. A difference from the varying surface temperature situation, is that the structure of the reactive zone does not change much with increasing Reynolds number, while the maximum reaction rate goes up, especially at the front stagnation point where the most violent reaction of gas phase occurs. Except for the contribution from an increase of the CO production from the surface reactions, the distribution of the Damköhler number (Da) in Figure 14 shows that both the convective and diffusive Damköhler number is always above one, meaning that the gas phase reaction is always transport-limited, and thus an increase of the velocity of incoming flow will provides much more oxygen to this reaction, leading to a faster gas phase reaction. Here, the convective *Da* is defined as

$$Da_{\mathrm{conv}} = \frac{\tau_{\mathrm{conv}}}{\tau_{\mathrm{chem}}} \tag{36}$$

where τ_{conv} is the convective time scale, defined as

$$\tau_{\mathrm{conv}} = \frac{d_p}{U_\infty} \tag{37}$$

The diffusion *Da* is

$$Da_{\mathrm{diff}} = \frac{\tau_{\mathrm{diff}}}{\tau_{\mathrm{chem}}}. \tag{38}$$

And

$$\tau_{\mathrm{diff}} = \frac{d_p^2}{D_{\mathrm{CO}}} \tag{39}$$

is diffusion time scale with D_{CO} being the CO diffusion coefficient in gas mixture

$$\tau_{\mathrm{chem}} = \frac{Y_{\mathrm{CO}}}{R_{(3)}} \tag{40}$$

is the characteristic time for chemistry. Another point worth of noting is that when the Reynolds number is above 5, the transport is controlled by diffusion instead of convection.

To investigate the local char conversions, three different angular positions at the surface are chosen for closer inspection. In Figure 15, the conversion rates of different species at the three angular positions are shown. Consistent with CO gas-phase conversion in the boundary layer, the stagnation point is still the most reactive zone for heterogeneous reactions. It is also seen that the reaction at the rear stagnation point is not sensitive to the Reynolds number.

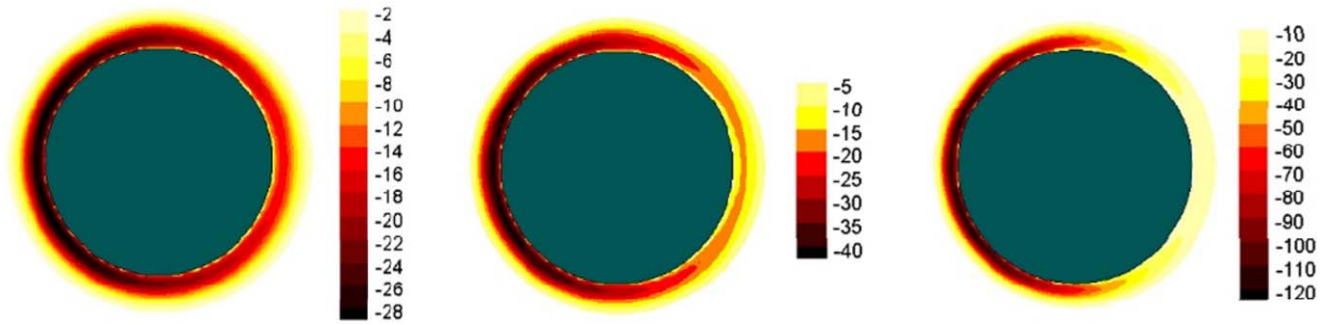

Figure 13. Reactive zones of gas-phase in terms of CO consumption rate.

[Color figure can be viewed at wileyonlinelibrary.com]

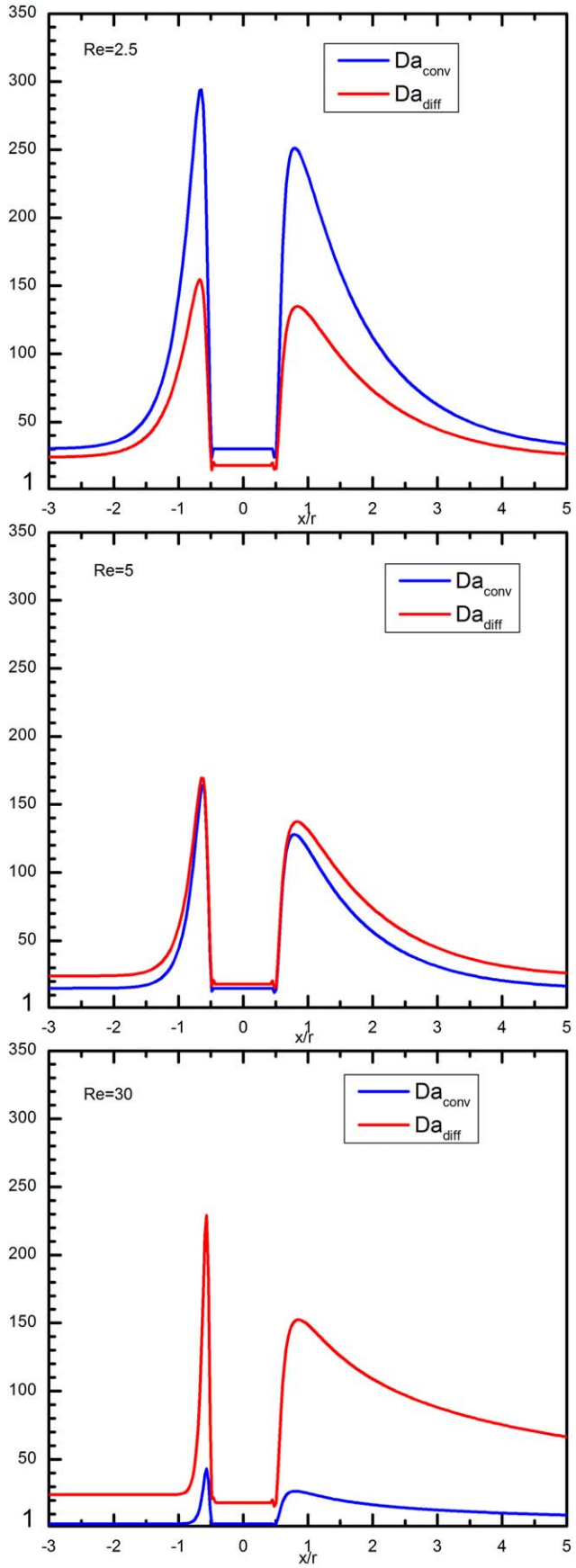

Figure 14. Distribution of convective and diffusive *Da* number along *x* at *y* = 0.

[Color figure can be viewed at wileyonlinelibrary.com]

Effect of Combustion on Mass, Momentum, and Energy Exchange. With heterogeneous and homogeneous reactions occurring on the solid surface and in the bulk gas, the temperature and species concentration in the gas mixture near the

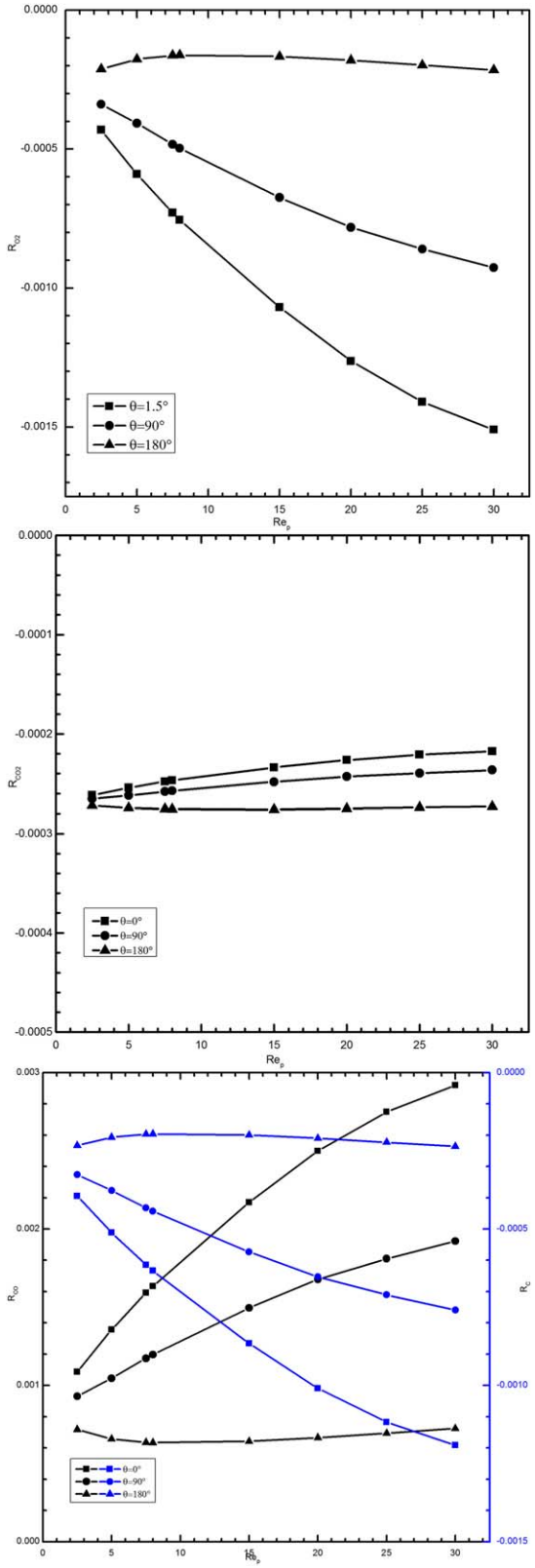

Figure 15. The local consumption or production rate of different species.

[Color figure can be viewed at wileyonlinelibrary.com]

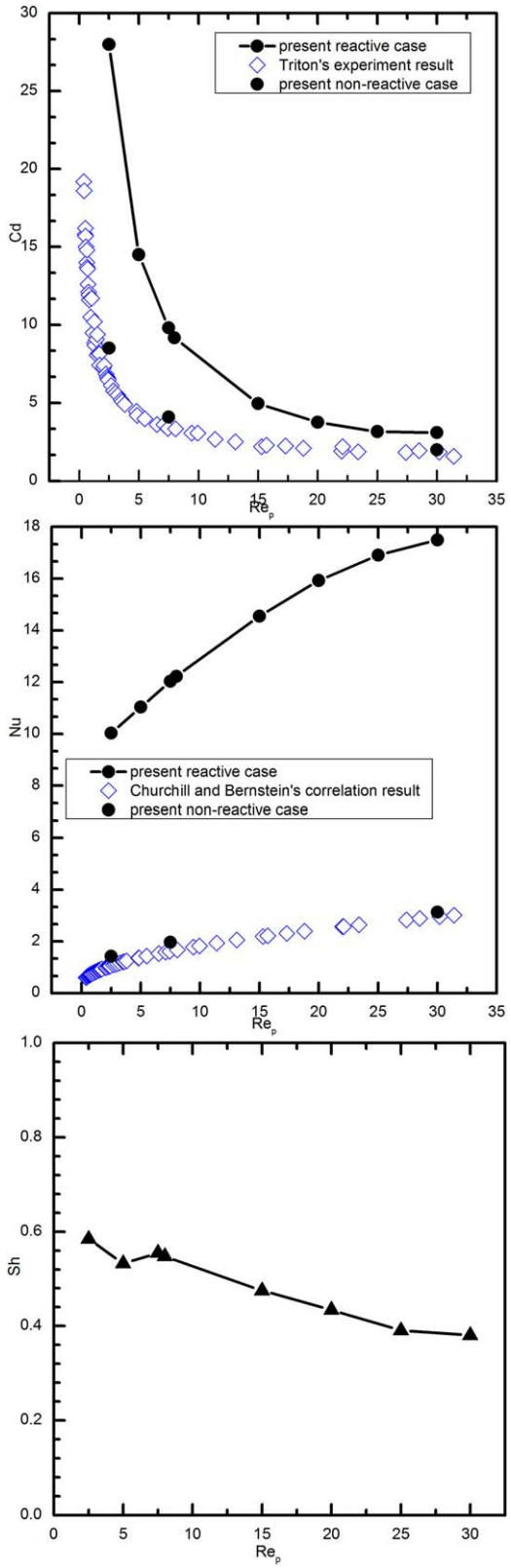

Figure 16. Evolution of C_d, Nu, and Sh number with Reynolds number.

[Color figure can be viewed at wileyonlinelibrary.com]

particle surface show a behavior that is different from a nonreactive situation. Hence, the fluid properties, such as dynamic viscosity and thermal conductivity, vary accordingly. In addition, the Stefan flow also changes the flow structure, leading to

Table 2. Averaged Dynamic Viscosity

	$v(g/(cm \cdot s))$		
Re	With Reactions	Without Reactions	Inlet Air
2.5	2.056784	1.960409	1.8255142
5	2.016095	–	
7.5	2.002146	1.918333	
8	1.999664	–	
15	1.974224	–	
20	1.963458	–	
25	1.957802	–	
30	1.956899	1.897289	

quite different velocity and temperature gradient distributions over the particle. Therefore, char conversion rates are expected to have a significant influence on both the drag force and the Nusselt number, which are the two main parameters used to calculate the exchange of momentum and energy between gas and solid phase. This effect is investigated in the following.

The drag force coefficient

$$c_d = \frac{F_{\text{drag}}}{\frac{1}{2}\rho U_\infty^2} \tag{41}$$

and the Nusselt number

$$Nu = \frac{\int_{\text{surf}} \nabla T \cdot \vec{n} ds}{T_s - T_\infty} \tag{42}$$

for situations with and without heterogeneous reactions are shown in Figure 16. The corresponding c_d and Nu from Triton's experimental results[41] and Churchill and Bernstein's correlation function[42]

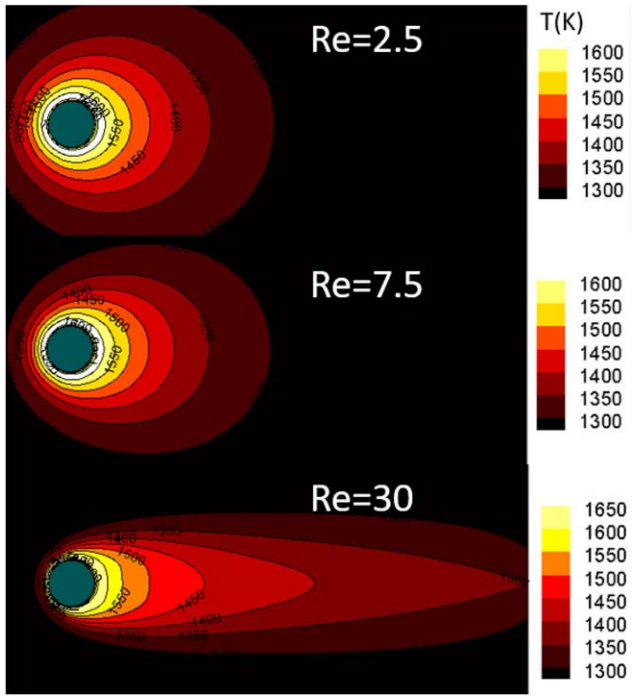

Figure 17. Temperature contour under different Reynolds numbers.

[Color figure can be viewed at wileyonlinelibrary.com]

$$Nu = 0.3 + \frac{0.62\mathrm{Re}^{1/2}}{\left[1+(0.4/\mathrm{Pr})^{2/3}\right]^{1/4}}\left[1+\left(\frac{\mathrm{Re}}{282000}\right)^{5/8}\right]^{4/5} \quad (43)$$

are also shown, respectively. It can be observed that the present nonreactive results (obtained by turning off the heterogeneous reactions) agree well with that in literatures. With a reactive solid surface, the drag force coefficient follows the same trend with increasing Reynolds number compared to that in the nonreactive situation. However, the magnitude is much higher. The underlying physical reasons are first investigated by comparing the averaged gas-phase viscosity (averaged over a $4d \times 4d$ square domain with the cylinder occupation excluded) and comparing them with the that for air at 1280 K and under 1 bar atmosphere. As is shown in Table. 2, the gas mixture becomes more viscous in the reactive situation due to the change of the mixture components and also the higher temperature. Other contributions to the increase of the drag force may include the change of the hydrodynamic boundary layer around the particle caused by the Stefan flow, as is shown by Dierich et al.[23] As a result of the heat release by gas-phase combustion in the boundary layer, a high temperature zone (shown in Figure 17) forms around the particle, resulting in a strong heat flux toward the solid surface, as is described by Figure 16. Moreover, a faster gas-phase reaction with a higher Reynolds number releases more heat, leading to a larger value of the Nusselt number. Finally, the evolution of the Sherwood number which is defined as

$$Sh = \frac{\int_{\mathrm{Surf}}\left(\sum_i^k \rho D_i \nabla Y_i\right) ds}{\rho \pi d \sum_i^k D_i\left(Y_{\mathrm{inlet},i} - Y_{\mathrm{surf},i}\right)} \quad (44)$$

is investigated in Figure 16. With increasing Reynolds number, the Sherwood number decreases, implying that to eject the same amount of mass into the gas flow more gas is transported to the solid surface and thus a low mass conversion efficiency.

Discussions and Conclusions

In this work, a novel ghost-cell immersed boundary method is proposed to describe the process of carbon burning. A convergence test shows that the current method can obtain a local second-order spatial accuracy. By comparing results from the present simulations with corresponding experimental results, the capability and accuracy of the present method is validated. The jump of the combustion rate of the graphite rod at about 1700 K is successfully captured. The physical reasons behind this phenomenon are explored. The change of the CO flame structure can be clearly observed, and consequently, the dominant surface reaction changes gradually from oxidation to gasification with increasing surface temperature. These findings agree well with conclusions by Makino et al.,[34] providing some validation that the present particle resolved IB method is suitable for a further investigation of char combustion. The results also imply that the double-film model may be more suitable than the single-film model when the surface temperature is high. Notably, Hecht et al.,[43] Gonzalo-Tirado et al.,[44,45] and Farazi et al.[46] also pointed out that the single-film assumption fails for large particles like that in the present simulation.

Based on the validations mentioned previously, the interaction between CO_2 gasification and O_2 oxidation introduced by varying Reynolds number are investigated as well as other char conversion properties. Results show that with increasing Reynolds number the contribution of O_2 oxidation to char consumption becomes more significant and the conversion rate of the char particle rises. By comparing this trend with the effect of surface temperature, it can be concluded that the solid surface temperature dominates over the Reynolds number when it comes to how to choose between single-film and double-film models for char conversion. Specifically speaking, the leading edge of the cylinder is the most reactive position for both surface and gas-phase chemistry. In the range of Reynolds numbers studied here, the gas phase reaction in the boundary layer is always transport-limited such that higher Reynolds numbers results in faster combustion.

Moreover, the effect of combustion on the exchange of mass, momentum, and energy between gas- and solid-phase is explored. Computational data indicates that a larger drag force is exerted on a solid particle that is embedded in a reactive environment. Heat release from the combustion in the boundary layer generates a high temperature sheet around the solid surface, causing a strong heat flux toward the burning surface. Even though, in the validation part, one can see that the solid surface temperature keeps decreasing, which means that radiation cannot be ignored in the energy conservation equation for the solid particle. By analyzing the Reynolds number dependence on the Sherwood number, one can find that higher Reynolds numbers lead to lower mass transfer efficiency, even with a fast char conversion rate.

It is concluded that the present GCCIB method is a powerful tool for fully resolved simulations of gas-solid flows with heterogeneous reactions. With the detailed information provided by such a simulation, one can improve the existing char conversion model and even develop new models. In the future, an extension of the present method to 3D particles under various conditions, such as oxy-fuel combustion and more detailed chemical mechanisms, will be explored.

Acknowledgment

This work is supported by the National Natural Science Foundation of China (Nos. 51390491, 51390493). Nils Haugen received funding from the European Union's Horizon 2020 research and innovation programme(No 764697). The project is also co-funded by the National Key Research and Development Plan of China (No. 2017YFE0112500).

Literature Cited

1. Nusselt W. Der verbrennungsvorgang in der kohlenstaubfeuerung. *Z Ver Dtsch Ing*. 1924;68:124–131.
2. Burke S, Schumann T. Kinetics of a type of heterogeneous reactions the mechanism of combustion of pulverized fuel. *Ind Eng Chem*. 1931;23(4):406–417.
3. Farazi S, Sadr M, Kang S, Schiemann M, Vorobiev N, Scherer V, Pitsch H. Resolved simulations of single char particle combustion in a laminar flow field. *Fuel*. 2017;201:15–28.
4. Peskin CS. Flow patterns around heart valves: a numerical method. *J Comput Phys*. 1972;10(2):252–271.
5. Peskin CS. The immersed boundary method. *Acta Numer*. 2003;11:1–39.
6. Haeri S, Shrimpton JS. On the application of immersed boundary, fictitious domain and body-conformal mesh methods to many particle multiphase flows. *Int J Multiphase Flow*. 2012;40:38–55.

7. Mittal R, Iaccarino G. Immersed boundary methods. *Annu Rev Fluid Mech*. 2005;37(1):239–261.
8. Sotiropoulos F, Yang X. Immersed boundary methods for simulating fluid–structure interaction. *Prog Aerosp Sci*. 2014;65:1–21.
9. Fadlun EA, Verzicco R, Orlandi P, Mohd-Yusof J. Combined immersed-boundary finite-difference methods for three-dimensional complex flow simulations. *J Comput Phys*. 2000;161(1):35–60.
10. de Tullio MD, De Palma P, Iaccarino G, Pascazio G, Napolitano M. An immersed boundary method for compressible flows using local grid refinement. *J Comput Phys*. 2007;225(2):2098–2117.
11. Berthelsen PA, Faltinsen OM. A local directional ghost cell approach for incompressible viscous flow problems with irregular boundaries. *J Comput Phys*. 2008;227(9):4354–4397.
12. Ghias R, Mittal R, Dong H. A sharp interface immersed boundary method for compressible viscous flows. *J Comput Phys*. 2007; 225(1):528–553.
13. Mittal R, Dong H, Bozkurttas M, Najjar FM, Vargas A, von Loebbecke A. A versatile sharp interface immersed boundary method for incompressible flows with complex boundaries. *J Comput Phys*. 2008;227(10):4825–4852.
14. Gilmanov A, Acharya S. A computational strategy for simulating heat transfer and flow past deformable objects. *Int J Heat Mass Transf*. 2008;51(17–18):4415–4426.
15. Gilmanov A, Sotiropoulos F. A hybrid cartesian/immersed boundary method for simulating flows with 3d, geometrically complex, moving bodies. *J Comput Phys*. 2005;207(2):457–492.
16. Shrivastava M, Agrawal A, Sharma A. A novel level set-based immersed-boundary method for CFD simulation of moving-boundary problems. *Numer Heat Transf B Fundam*. 2013;63(4):304–326.
17. Kim J, Choi H. An immersed-boundary finite-volume method for simulation of heat transfer in complex geometries. *KSME Int J*. 2004;18(6):1026–1035.
18. Luo K, Zhuang Z, Fan J, Haugen NEL. A ghost-cell immersed boundary method for simulations of heat transfer in compressible flows under different boundary conditions. *Int J Heat Mass Transf*. 2016;92:708–717.
19. Luo K, Mao C, Zhuang Z, Fan J, Haugen NEL. A ghost-cell immersed boundary method for the simulations of heat transfer in compressible flows under different boundary conditions Part-II: Complex geometries. *Int J Heat Mass Transf*. 2017;104:98–111.
20. McGurn MT, Ruggirello KP, DesJardin PE. An Eulerian–Lagrangian moving immersed interface method for simulating burning solids. *J Comput Phys*. 2013;241:364–387.
21. Kedia KS, Safta C, Ray J, Najm HN, Ghoniem AF. A second-order coupled immersed boundary-SAMR construction for chemically reacting flow over a heat-conducting cartesian grid-conforming solid. *J Comput Phys*. 2014;272:408–428.
22. Deen NG, Kuipers JAM. Direct numerical simulation of fluid flow accompanied by coupled mass and heat transfer in dense fluid–particle systems. *Chem Eng Sci*. 2014;116:645–656.
23. Dierich F, Richter A, Nikrityuk P. A fixed-grid model to track the interface and porosity of a chemically reacting moving char particle. *Chem Eng Sci*. 2018;175:296–305.
24. Brandenburg A, Dobler W. Pencil: Finite-difference code for compressible hydrodynamic flows. *Astrophysics Source Code Library*, 2010.
25. Babkovskaia N, Haugen NEL, Brandenburg A. A high-order public domain code for direct numerical simulations of turbulent combustion. *J Comput Phys*. 2011;230(1):1–12.
26. Wilke CR. A viscosity equation for gas mixtures. *J Chem Phys*. 1950;18(4):517–519.
27. Coffee TP, Heimerl JM. Transport algorithms for premixed, laminar steady-state flames. *Combust Flame*. 1981;43:273–289.
28. Mourits FM, Rummens FHA. A critical evaluation of Lennard–Jones and Stockmayer potential parameters and of some correlation methods. *Can J Chem*. 1977;55(16):3007–3020.
29. Strohle J, Myhrvold T. An evaluation of detailed reaction mechanisms for hydrogen combustion under gas turbine conditions. *Int J Hydrogen Energy*. 2007;32(1):125–135.
30. Kee RJ, Miller JA, Jefferson TH. CHEMKIN: A general-purpose, problem-independent, transportable, FORTRAN chemical kinetics code package. *Sandia Labs*., 1980.
31. Kee RJ, Coltrin ME, Glarborg P. *Chemically Reacting Flow: Theory and Practice*. Newark, NJ: Wiley, 2003.
32. Zhang L, Liu K, You C. Fictitious domain method for fully resolved reacting gas–solid flow simulation. *J Comput Phys*. 2015;299:215–228.
33. Nikrityuk PA, Gräbner M, Kestel M, Meyer B. Numerical study of the influence of heterogeneous kinetics on the carbon consumption by oxidation of a single coal particle. *Fuel*. 2013;114:88–98.
34. Makino A, Namikiri T, Kimura K. Combustion rates of graphite rods in the forward stagnation field with high-temperature airflow. *Combust Flame*. 2003;132(4):743–753.
35. Walls JR, Strickland-Constable RF. Oxidation of carbon between 1000–2400°c. *Carbon*. 1964;1(3):333–338.
36. Yoo CS, Im HG. Characteristic boundary conditions for simulations of compressible reacting flows with multi-dimensional, viscous and reaction effects. *Combust Theory Model*. 2007;11(2):259–286.
37. Yang RT, Steinberg M. A diffusion cell method for studying heterogeneous kinetics in the chemical reaction/diffusion controlled region. Kinetics of $C + CO_2 \rightarrow 2CO$ at 1200–1600°C. *Ind Eng Chem*. 1977; 16:235–242.
38. Makino A, Araki N, Mihara Y. Combustion of artificial graphite in stagnation flow: Estimation of global kinetic parameters from experimental results. *Combust Flame*. 1994;96(3):261–274.
39. Hees J, Zabrodiec D, Massmeyer A, Pielsticker S, Gövert B, Habermehl M, Hatzfeld O, Kneer R. Detailed analyzes of pulverized coal swirl flames in oxy-fuel atmospheres. *Combust Flame*. 2016; 172:289–301.
40. Richter A, Nikrityuk PA, Kestel M. Numerical investigation of a chemically reacting carbon particle moving in a hot o2/co2atmosphere. *Ind Eng Chem Res*. 2013;52(16):5815–5824.
41. Tritton DJ. Experiments on the flow past a circular cylinder at low Reynolds numbers. *J Fluid Mech*. 1959;6(04):547
42. Churchill SW, Bernstein M. A correlating equation for forced convection from gases and liquids to a circular cylinder in crossflow. *J Heat Transf*. 1977;99(2):300.
43. Hecht ES, Shaddix CR, Lighty JS. Analysis of the errors associated with typical pulverized coal char combustion modeling assumptions for oxy-fuel combustion. *Combust Flame*. 2013;160(8):1499–1509.
44. Gonzalo-Tirado C, Jiménez S. Detailed analysis of the co oxidation chemistry around a coal char particle under conventional and oxy-fuel combustion conditions. *Combust Flame*. 2015;162(2):478–485.
45. Gonzalo-Tirado C, Jiménez S, Johansson R, Ballester J. Comparative study of four alternative models for co oxidation around a burning coal char particle. *Combust Flame*. 2014;161(4):1085–1095.
46. Farazi S, Sadr M, Kang S, Schiemann M, Vorobiev N, Scherer V, Pitsch H. Variable transport coefficients effects on the single-film model of char combustion. *Combust Meet Eur*. 2017;201:15

Manuscript received July 13, 2017, and revision received Jan. 12, 2018.